An experimental investigation into the flow mechanics of dimpled surfaces in turbulent boundary layers

Van Campenhout, Olaf W.G.; Van Nesselrooij, Michiel; Veldhuis, Leo L.M.; Van Oudheusden, Bas W.; Schrijer, Ferdinand F.J.

DOI
10.2514/6.2018-2062

Publication date
2018

Document Version
Final published version

Published in
AIAA Aerospace Sciences Meeting

AIAA SciTech Forum
8–12 January 2018, Kissimmee, Florida
2018 AIAA Aerospace Sciences Meeting

10.2514/6.2018-2062

An experimental investigation into the flow mechanics of dimpled surfaces in turbulent boundary layers

Olaf W.G. van Campenhout*, Michiel van Nesselrooij†, Leo L.M. Veldhuis‡,
Bas W. van Oudheusden§, Ferdinand F.J. Schrijer¶
Delft University of Technology, Delft, the Netherlands

Although various experimental studies have confirmed the potential drag reducing effect of dimpled surfaces in a turbulent boundary layer, the working mechanism remains largely unresolved. An experimental investigation has been performed with the objective to strengthen the understanding of this aerodynamic surface and its interaction with the turbulent boundary layer. Direct force measurements were combined with Particle Image Velocimetry (PIV) and Particle Image Surface Flow Visualization (PISFV). The direct force measurements reveal that the drag reduction is highly sensitive to flow conditions: a finding with significant implications for further research as well as for potential applications. Furthermore, the PIV and PISFV measurements reveal a spanwise oscillation of the flow near the surface due to the interaction of individual dimple flow topologies, which are of the converger-diffuser type. The measurement of this oscillation provides evidence for a novel drag reduction theory: the interaction between dimples causes alternating spanwise excitations of the near-wall flow which interacts with the turbulent coherent structures which leads to a reduction of the turbulent drag.

Nomenclature

English Symbols

d	Dimple depth
D	Dimple diameter
h	FOV height relative to the wall
L_x,L_z	Streamwise, spanwise dimple spacing
N	Number of vector fields
r	Dimple edge curvature radius
t^+	Dimensionless time since start
T^+	Dimensionless period
u,v,w	Velocity in x, y, z
u',v',w'	RMS of fluctuations in u, v, w
U_∞	Free stream flow velocity
w^+	Dimensionless w
w_m^+	Maximum w^+
W_m^+	Dimensionless maximum wall velocity
x,y,z	Streamwise, wall-normal and spanwise coordinates
y^+	Dimensionless wall-normal coordinate

Greek symbols

δ	Boundary layer thickness
Δt	Laser pulse separation time
ϵ_u,ϵ_w	Instantaneous PIV vector error in u, w
$\epsilon_{u'}$,$\epsilon_{w'}$	PIV error in RMS vector field u', w'
$\epsilon_{\overline{u}}$,$\epsilon_{\overline{w}}$	PIV error in mean vector field of u, w

Dimensionless groups

C_D	Drag coefficient based on free stream flow conditions and test plate top area
Re_δ	Reynolds number based on δ and the friction velocity
Re_τ	Reynolds number based on half of the channel height and the friction velocity
Re_D	Reynolds number based on dimple diameter and free stream flow conditions

*MSc. Aerospace Engineering, Department of Aerospace Engineering, Section of Aerodynamics
†MSc. Aerospace Engineering, Department of Aerospace Engineering, Section of Aerodynamics
‡Professor, Department Aerospace Engineering, section of Flight Performance and Propulsion
§Associate Professor, Department of Aerospace Engineering, Section of Aerodynamics
¶Assistant Professor, Department of Aerospace Engineering, Section of Aerodynamics

I. Introduction and background

Any reduction in vehicle drag or fluid resistance provides a potential of substantial energy savings, with obvious benefits to the economy, environment and overall industrial competitiveness. Over the years, various means of passive flow control have emerged that could potentially reduce drag significantly.[1–3] Examples are, among others, natural laminar flow (NLF), riblets, large eddy break-up devices (LEBUs), compliant coatings and wavy walls. These techniques have been studied for many years, but they have not found their way into large-scale commercial applications, for example, due to their impact on vehicle design and/or maintainability. A potential alternative passive flow control technique aimed at turbulent drag reduction is the dimpled surface. Various experimental studies on this technique have been reported, suggesting that dimpled surfaces have a serious potential for turbulent drag reduction. Research by Tay has shown a drag reduction over dimpled surfaces in a channel flow of up to 3%,[4] while research at Delft University of Technology (DUT) was reported to achieve a drag reduction of 5-10% for a dimpled plate compared to a flat plate.[5]

Kiknadze has performed research on dimpled surfaces for many years, with initial focus on the heat transfer enhancement effect, and presents the formation of vortices in the dimples as the key mechanism for drag reduction.[6] He argues that these vortices could act as fluid-dynamic ball-bearings to the flow and/or induce a positive shear force in the regions of reversed flow. In latest research at DUT, van Nesselrooij found that relatively shallow dimples oriented in a certain pattern can yield a drag reduction of up to 4% at a Re_D of up to 40,000.[7] Furthermore, he has shown using Particle Image Velocimetry (PIV) that there is no significant vortex generation in these drag reducing dimples. Lastly, van Nesselrooij has built a hypothesis on the generation of spanwise shear as the main mechanism for drag reduction. This "Spanwise Shear" hypothesis has also been put forward recently by Tay.[4] At this stage, however, there is no clear consensus on what constitutes the drag reducing mechanism caused by dimpled surfaces. Therefore, an experimental study was performed with the specific objective to verify previously obtained drag results and provide detailed flow visualizations, which may lead to a better understanding of the drag reducing mechanism of these dimpled surfaces. Direct force measurements are combined with PIV and Particle Image Surface Flow Visualization (PISFV).

II. Experimental setups

The measured surfaces consist of spherical dimples which are completely described by the following parameters: diameter (D), depth (d), edge curvature radius (r), center-to-center streamwise dimple spacing (L_x), spanwise dimple spacing (L_z) and the chosen configuration (staggered or aligned). The dimple design and configuration definition are depicted in Figure 1. The dimple design parameters are based on the design of the dimples which has previously shown drag reductions at DUT.[7] An overview of tested dimple design parameters can be found in Table 1.

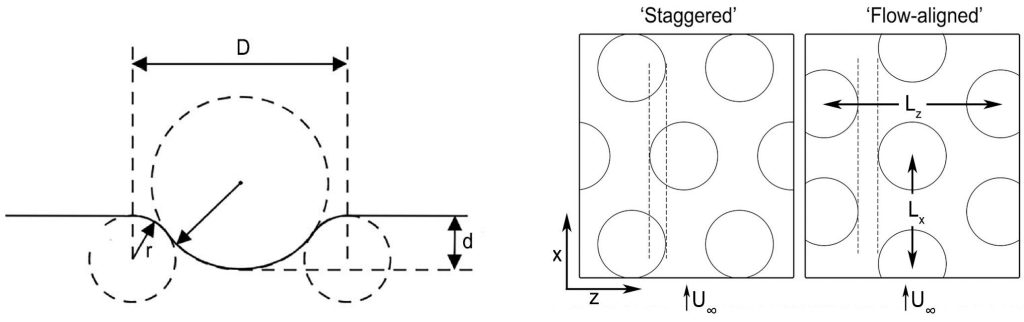

Figure 1. Cross-section of a dimple (left).[7] The dimple depth is exaggerated. Streamwise and spanwise dimple spacing (L_x, L_z) and the definition of a staggered and flow-aligned dimple pattern (right).[7]

Table 1. Overview of tested dimple design parameters.

D [mm]	d [mm]	r [mm]	L_X [mm]	L_Z [mm]	Configuration
20	0.5	10	57.18	33	Staggered

Two test models have been used: **1) Passive dimples**, a dimpled plate has been manufactured by milling the dimples into a Polyoximethylene (POM) plastic plate with size of 669x351 mm. This is the same model with which previously drag reductions at DUT were obtained and hence measurements over this model can be used to verify previous results.[7] Furthermore, a flat plate with the same dimensions is manufactured from the same material for reference measurements. **2) Active dimples**, a custom design has been made for an actively dimpled plate. The working principle of the active dimples is based on a vacuum driven elastic foil deformation. The dimples are milled out of aluminum with a small vacuum channel in center of each. A sheet of 2 mm thick Polyurethane (PU) rubber Shore-A 90 is then glued over the dimple. By applying a vacuum, the dimple is activated. A schematic overview of this operation principle can be found in Figure 2. The active dimples model can be transformed into a flat reference plate without changing the setup, hence minimizing errors associated to plate replacement and/or reassembly of the setup. Furthermore, the model allows for the testing of various patterns by selectively activating the dimples.

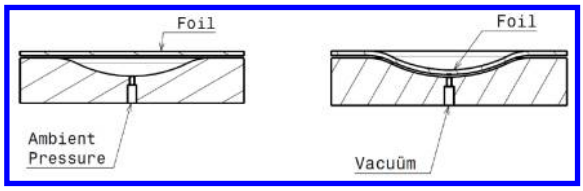

Figure 2. Schematic of active dimple operating principle. Note that this schematic is not to scale with the actual dimple used in this research.

By means of a Konica Minolta VIVID 700 Laser-Time-Of-Flight 3D scanner, it has been verified that both dimple shapes do not vary substantially from the design (nominal dimple depth of 500 μm): the average Root Mean Square Error (RMSE) between the design and the mean of six measurements over the dimple centerlines are 82 μm and 45 μm for the active and passive dimples respectively. As a consequence of the wind tunnel assembly, the test models have been subjected to two different pressure gradients in the inflow region upstream of the dimpled plates: **1) FPG**, by means of two inlays in the wind tunnel, the maximum free stream flow velocity can be increased while creating a Favorable Pressure Gradient (FPG) upstream of the test model. **2) ZPG**, the test plates can also be fitted in the wind tunnel such that there is almost no pressure gradient at the inflow, hence resembling Zero Pressure Gradient (ZPG) inflow. This is the exact same setup that previously obtained drag reductions at DUT.[7] The difference in inflow geometry is depicted in Figure 3.

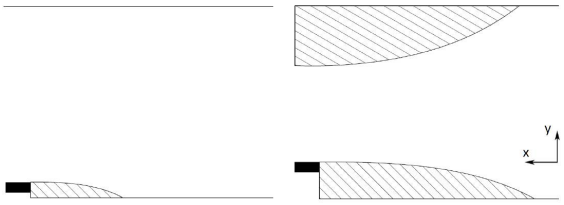

Figure 3. Inflow cross section for ZPG (left) and FPG (right). Hatched area indicates area reduction and solid area indicates start of test model. Flow from the right and the boundary layer is tripped by means of carborundum roughness elements (with an average diameter 0.5 mm) directly at the start of the lower area reducing element.

Previous research at DUT has shown that the measured drag reduction increases with increasing Reynolds number.[7] This Reynolds number dependency of the drag reduction makes investigations of the higher Reynolds number regime interesting. Hence, the direct force measurements will be performed at inflow FPG so the tested velocity regime can be extended from 5-30 m/s as in the previous research[7] to 6-50 m/s in the current research. Flow visualizations were performed for the ZPG which corresponds with the conditions where a drag reduction was previously measured. Table 2 presents which measurement technique is performed on which test model and at which inflow pressure gradient.

Table 2. Experimental setup matrix of inflow pressure gradient versus test models

	FPG at inflow	**ZPG at inflow**
Passive dimples	Direct force measurements	PIV & PISFV
Active dimples	Direct force measurements	-

II.A. Drag measurement setup

The models are tested in a low-speed wind tunnel, which has a cross section of 20x40 cm for flow speeds up to 50 m/s (with inflow FPG). A schematic overview of the setup which was used to perform the direct force measurements for the active dimples can be found in Figure 4. The inflow cross section of the wind tunnel test section (A) is decreased by a top wall inlay (B) and a leading edge (LE) ramp (C). The free stream flow velocity over the plate is measured by means of a pitot tube (D). The active dimples model (E) is supported by a puck air bearing (F) and a linear air bearing (G). The linear air bearing constrains the movement of the model to the streamwise direction and is connected directly to the force sensor (H), a KD40S-2N by ME-Meßsysteme with a rated accuracy of 0.05%. At the trailing edge, a horizontal element (I) guides the flow towards the exit of the tunnel. The pressure measurements are performed using DPG 2101 pressure sensors by Mensor with a stated accuracy of 0.03%. The temperature is recorded with a DTM 5080 by LKM Electronic with a stated accuracy of 0.02 degrees Celcius. The vacuum pump is of the type D2A by Leybold Heraeus and the high pressure air is supplied by a ZSG 315 compressor by ALUP GrassAir.

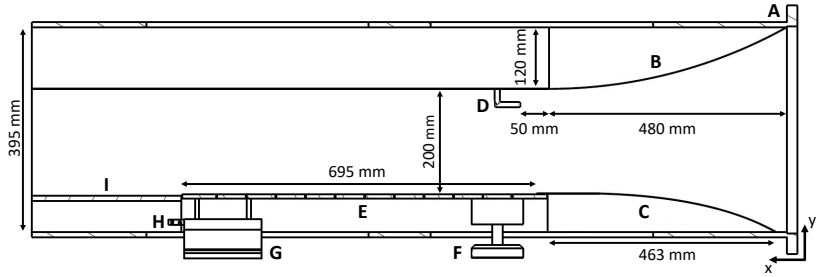

Figure 4. Schematic side view of direct force measurement setup for active dimples. A) Wind tunnel test section, B) Area reducing inlay, C) Area reducing ramp, D) Pitot tube, E) Active dimples model, F) Puck air bearing, G) Linear air bearing, H) Force sensor, and I) Rear flow guide. Flow from the right.

Seven different dimple patterns were tested, as depicted in Figure 5. The pattern with all dimples activated is indicated as pattern 1 and has the exact same geometry as the passive dimples model. Every measurement consists of measuring the drag at 6-50 m/s with 2 m/s increments resulting in 23 measurement points. Individual measurements are logged at 10,000 Hz for 10 seconds resulting in 100,000 data points per velocity increment. All patterns are measured three times and referenced against flat plate measurements. Using the three measurements, the mean and the RMSE of the drag difference is computed for every pattern with respect to the flat plate. By means of Welch's t-test, the statistical confidence interval of all measured drag differences was shown to be at least 99.99%. Also, by means of 8 subsequent flat plate repeatability measurements, it was shown that the average RMSE over the entire Re_D domain was 0.47% (expressed as percentage of the average C_D of all measurements). Furthermore, the effect of turning the air bearings on and off was evaluated for all loadings of the model. For this verification measurement, the average RMSE over the entire Re_D domain was 0.57% (expressed as percentage of the average C_D of all measurements). Also, the boundary layer was verified to be turbulent by means of a traversing pivot tube at the LE, the shape factor was found to be below 1.3 for the entire Re_D domain (with δ for the active dimples setup of 11.1, 9.7, and 9.45 mm for Re_D of 6700, 40000 and 65000 respectively). The effect of drift was measured by computing the RMSE between all flat plate measurements. For this verification, the average RMSE over the entire Re_D domain was 0.57% (expressed as percentage of the average C_D of all measurements).

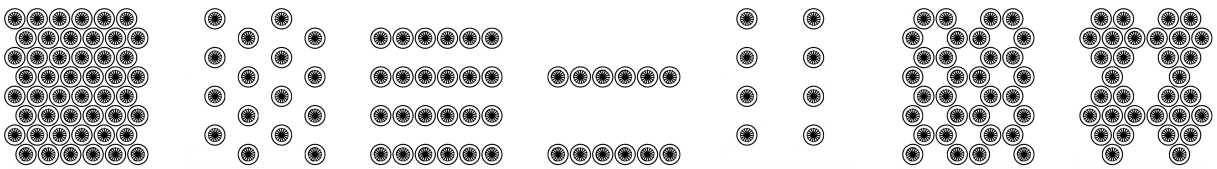

Figure 5. Dimple patterns 1-7. Note that this figure depicts the dimples as well as the outer rings were the adhesive can be applied, the inner circle indicates the dimple. Pattern numbering (1-7) from left to right and flow from below.

The direct force measurement setup for the passive dimples is identical to that of the active setup, as described in the foregoing description, except for two differences: 1) the linear air bearing (G) is moved to the streamwise center of the model and the puck air bearing (F) is removed. 2) The dimpled plate measurement is performed between two flat plate measurements following the best practices by van Nesselrooij.[7]

II.B. PIV setup

To perform the PIV measurements, a laser sheet is directed into the test section from the open downstream end of the wind tunnel. The laser sheet is oriented horizontally and parallel with the free stream flow direction and has a width of approximately 1.5 mm at the measurement location. The setup is used to investigate the flow at a free stream velocity of 30 m/s since previous research has indicated the highest drag reduction at these velocities. Both the drag reducing plate as well as the flat reference plate have been investigated. The field of view (FOV) for the setup is aligned horizontally with the test plate and is schematically illustrated in Figure 6. The flow topology is visualized in three planes to allow the reconstruction of the flow field statistics across the boundary layer. This is achieved by traversing the laser optics and camera across a rail simultaneously. The FOV is located at the streamwise and spanwise centre of the model. The camera is fitted with a Scheimpflug adapter, which positions the lens at an angle of approximately 5 degrees relative to the camera sensor. Details on FOV height relative to the wall (h), FOV size, spatial resolution, vector pitch and pulse separation time are given in Table 3.

Table 3. PIV configurations for all three planes. y^+ is calculated based on an estimated friction velocity of 1.235 after previous PIV measurements by van Nesselrooij.[7]

ID	h [mm]	h (y^+)	h (y/δ)	FOV [mm]	px/mm	Pitch [mm]	Δt [μs]
1	3	243	0.2	56x80	20	0.28	13
2	8	648	0.5	56x80	20	0.28	13
3	13	1053	0.9	56x80	20	0.28	13

The recording equipment consists of of a CCD Imager LX 16M camera by LaVision with 4904x3280 px sensor fitted with Scheimpflug and AF Micro Nikkor 110 mm lense. The aperture has been set to f/8 for all the measurements. Illumination is provided by a double-pulsed ND:Yag Evergreen laser by Quantel, type 200. The seeding is achieved using a Safex fog generator. Each measurement consists of 1000 image pairs, which are acquired at 0.5 Hz. This acquisition rate allows for statistical characterization of the flow, however it is insufficient to capture time-resolved turbulence. The LaVision DAVIS 8.3 software is used for camera and laser control in combination with a LaVision programmable timing unit (PTU). The LaVision DAVIS 8.3 software is used for PIV data processing. The PIV processing is performed using an interrogation window of 96x96 px and a 50% overlap in the first iteration followed by two iterations based on 4:1 elliptical interrogation windows (equivalent window size of 32x32 px) with 75% overlap. The final vector spacing is 0.28 mm for all results. The instantaneous in-plane velocity vector errors are estimated based on an estimated 0.1 pixel correlation factor after Raffel and the average pixel displacement in the various planes.[8] The uncertainty in the mean and RMS vector field as obtained from N flow fields is determined following the methodlogy by Benedict.[9] The resulting error estimates can be found in Table 4.

Table 4. PIV velocity uncertainty estimates expressed as $\%U_\infty$.

Plane	ϵ_u	ϵ_w	$\epsilon_{\overline{u}}$	$\epsilon_{\overline{w}}$	$\epsilon_{u'}$	$\epsilon_{w'}$
1	0.91	0.91	0.41	0.33	0.29	0.23
2	0.77	0.77	0.24	0.19	0.17	0.13
3	0.63	0.63	0.35	0.29	0.25	0.20

II.C. PISFV setup

The PISFV setup is used to investigate the flow at a free stream velocity of 30 m/s. Both the drag reducing plate as well as the flat reference plate are investigated. The FOV for the setup spans multiple dimples and is schematically illustrated in Figure 6. Details on FOV size, spatial resolution, vector pitch and acquisition frequency are given in Table 5.

Table 5. PISFV configuration.

FOV [mm]	px/mm	Vector pitch [mm]	Acquisition frequency [Hz]
60x64	33.32	0.97	1

The experimental setup for the PISFV measurement campaign utilizes one CCD Imager LX 16M camera by LaVision with 4904x3280 px sensor fitted with an AF Micro Nikkor 110 mm lens. The aperture has been set to f/2.8 for all the measurements. The same oil as in traditional oil flow visualization is used, in this case Shell Ondina 68 Oil. Particles are based on fluorescent chalk which is strained to reduce particle size. The particles are illuminated using a blacklight. The LaVision DAVIS 8.3 software is used for camera control in combination with a LaVision PTU. Each measurement consists of a time-series of 200 images, which are acquired at 1 Hz. This acquisition rate allows for time resolved tracking of the oil film movement. Three measurements are performed over both the flat plate and the dimpled plate. The LaVision DAVIS 8.3 software is used for PISFV data processing. Due to the low signal to noise ratio and oversampled images during the PISFV measurements, a time-resolved multi-frame pyramid correlation scheme is particularly well suited and is used.[10] The cross-correlation processing is performed using an interrogation window of 256x256 px and a 50% overlap in the first iteration followed by three iterations based on circular interrogation windows (equivalent window size of 128x128 px) with 75% overlap. The final vector spacing is 0.97 mm for all results. It is verified that the oil layer is sufficiently thin with respect to the dimple depth (500 μm). To verify this, first the oil layer thickness is estimated at application based on the application area, oil density and the measured weight of the applied oil. Furthermore, the thinning of the oil layer during the measurements is calculated by using the average particles per pixel as a proxy (by means of a linear regression). It is estimated that the oil layer is between 7-10 μm when the PISFV measurements are performed. Mosharov suggests that an oil layer for surface oil flow visualizations is typically 20 μm thick.[11]

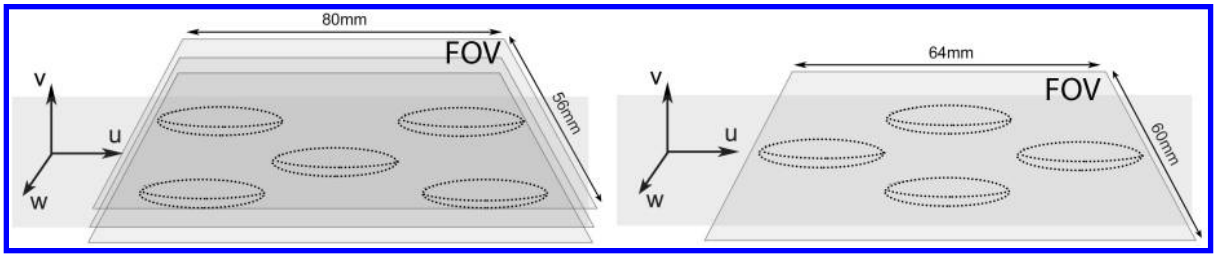

Figure 6. Schematics of vertical 2C PIV FOV planes (left) and the PISFV FOV (right).

III. Results

The direct force measurement results for the active dimples (pattern 1) and the passive dimples can be found in Figure 7. The other tested active dimple patterns show similar results and have therefore not been depicted. As can be observed, a marginal drag increase (approximately 1% over the entire Re_D domain) is observed for both the passive and the active dimples. Furthermore, the results are repeatable as can be observed from the rather narrow RMSE bandwidth (approximately 1% of C_D on average over entire Re_D domain). The measurements are sufficiently repeatable as to detect statistically significant drag differences of approximately 1%. Note that in contrast to the present findings, previous literature suggests that a 0-4% drag reduction is to be expected.[7]

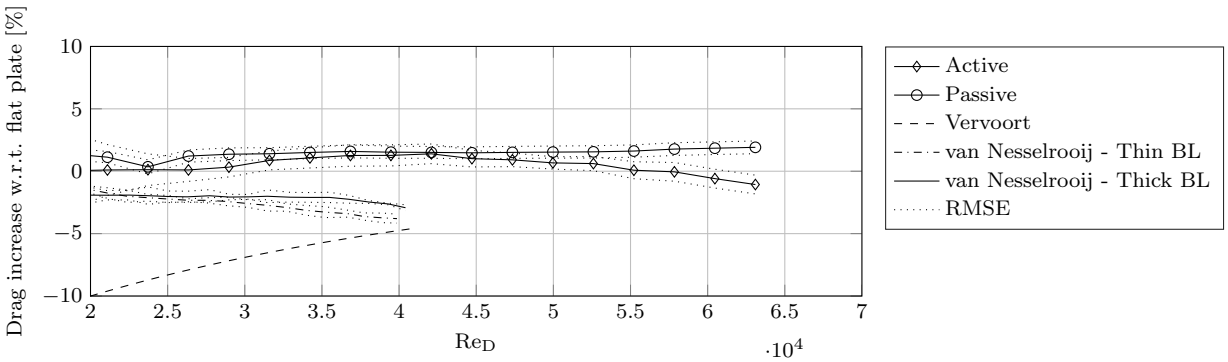

Figure 7. Drag delta due to pattern 1 for the active dimples at FPG and the passive dimples at FPG plotted against results for the same geometry by van Nesselrooij[7] and a very similar geometry by Vervoort.[5] Dotted line indicates RMSE and data points indicate sampled Re_D.

Figure 8 presents the results for the PIV and the PISFV measurements. As can be observed from the PIV results, as the flow enters a dimple, the flow converges into the dimple and diverges again at the downstream half of the dimple. This flow topology is visible in all dimples that lie within the FOV. The average change in spanwise velocity between the dimpled and flat plate is in the order of 1-2% of the free stream flow velocity. It has to be noted however, that these values are in the order of the errors as presented in Table 4. Due to the pattern of dimples, the regions of positive/negative spanwise velocity meander in an oscillatory manner over the surface. The PIV results at plane 2 and 3 do not show this oscillatory flow topology and hence have not been depicted. The observed flow topology is confirmed by the PISFV results.

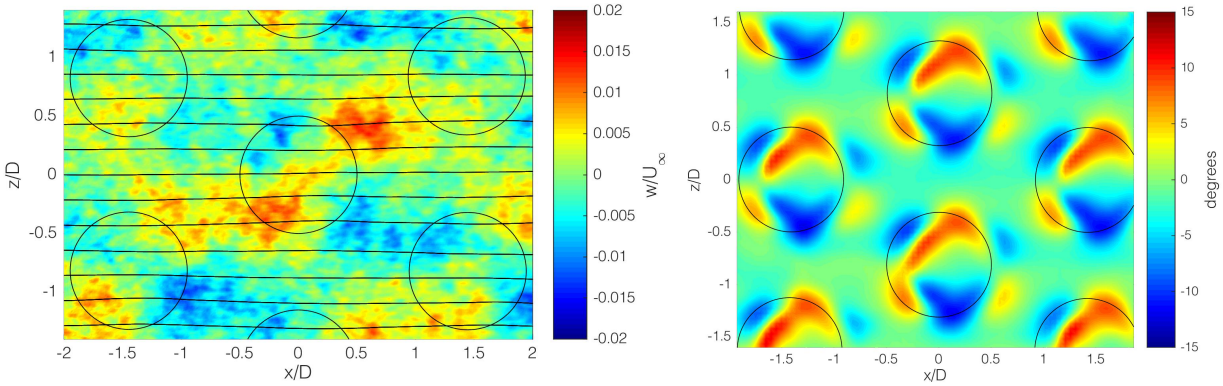

Figure 8. Spanwise mean velocity contour over the dimpled plate at plane 1 as obtained using PIV (left). Flow from the left and U_∞ = 30 m/s. Flat plate data is subtracted and w-component in streaklines is amplified 5x for clarity. Local vector angle (anti-clockwise positive) with respect to the free stream flow velocity obtained using PISFV (right). Mean of three measurements (each measurement consists of a time-series of 200 images) of the dimpled plate. Flow from the left and U_∞ = 30 m/s.

IV. Discussion

As can be observed from Figure 7, no drag reduction is found. If anything can be concluded from the balance measurements, a marginal drag increase is observed for all configurations. This is remarkable since pattern 1 from the active dimple model as well as the passive dimple model are based on exactly the same geometry as used in the research by van Nesselrooij.[7] The possible differences are investigated to determine if there are any substantial differences in the current and previous setup which could lead to different skin friction measurements. First of all, the same wind tunnel is used. Secondly, a similar Re_D regime is tested and the boundary layer has been shown to be turbulent and of similar thickness. Lastly, the passive dimple model is the same model as used in the previous research. There is however, one substantial difference when comparing the current to the old setup: the inflow boundary layer is subject to a strong favorable pressure gradient (FPG) in the current setup and to almost no pressure gradient in the old setup (ZPG).

The hypothesis reconciled by the current research for the drag-reducing mechanism of a dimpled surface as described by Tay and van Nesselrooij is based on spanwise excitations of the near-wall flow.[4,7] It states that the dimples cause alternating spanwise excitations of the near-wall flow which interact with the coherent structures and therefore reduce the turbulent drag. This pattern bears resemblance to the alternating spanwise shear layer which is developed by oscillating the wall in spanwise direction, thereby creating a Stokes layer.[12] The coherent structures in a turbulent boundary layer are a key element of this hypothesis and literature indicates that coherent structures in a turbulent boundary layer are affected significantly by the streamwise pressure gradient.[13] Specifically, literature suggests that a FPG suppresses large-scale coherent structures while moving to a ZPG and subsequently to an APG promotes the large-scale coherent structures, both in occurrence and size.[14,15] Based on this dependency, it is therefore proposed that the difference in skin friction drag measurements is due to the difference in inflow pressure gradient. Specifically, the FPG from the current setup has suppressed the growth of the coherent structures in the turbulent boundary layer and this has rendered the drag reducing mechanism inoperable. It is expected that the converger-diffuser flow structures still exist over the dimpled surface, but that the excitation of the near-wall flow in spanwise direction does not significantly alter the skin friction drag. A marginal drag increase in the current measurements is therefore also expected since the pressure drag increases due to the dimples.

The results from the PIV and PISFV measurements give a representation of the flow field in the turbulent boundary layer over a drag reducing dimpled surface. As can be observed from Figure 8, the PIV results clearly show a converger-diffuser flow topology over the dimples in the near-wall plane ($y/\delta = 20\%$) as well as in the PISFV results. These results are in correspondence with earlier DUT results as described by van Campenhout.[16] Furthermore, in his overview of flow structures over dimples, Tay also predicts this flow topology (and named it stage 1 flow) for the current dimples at the tested Re_D regime.[17] The current PIV results of plane 2 ($y/\delta = 53\%$) and plane 3 ($y/\delta = 87\%$) do not show this flow topology. This is also in correspondence with literature since van Nesselrooij has shown that the converger-diffuser flow topology extends to heights of 0.1-0.2D above the surface (plane 1 is at a height of 0.15D).[7] The fact that this flow topology is only present in the near-wall region is expected in view that the surface modifications are relatively shallow ($d/\delta \approx 3\%$). Another interesting observation from the PIV and PISFV results is the absence of flow reversal. No region of reversed flow is observed in any of the available instantaneous vector fields from the PISFV or PIV measurements. The current results therefore challenge the drag reducing theories as set out by Kiknadze.[6]

The "Spanwise Shear" drag reduction theory as independently postulated by Tay and van Nesselrooij is based on the generation of spanwise oscillations in the near-wall flow due to the interaction of the converger-diffuser flow fields of the individual dimples.[4,7] The lateral excitation of the turbulent boundary layer would then lead to a drag reduction, in analogy to the drag reduction due to an active wall oscillation. The generation of these spanwise waves over dimpled surfaces has, however, never been measured and the hypotheses from literature were based on speculation of such oscillation. The current measurements are therefore the first to capture a near-wall oscillation over a drag reducing dimpled surface, as can be observed from Figure 8. Besides a confirmation of the occurrence of a spanwise oscillation in the near-wall flow, the current results also present the possibility for a quantification of this spanwise oscillation. As can be observed from Figure 8, not all streaklines follow the same oscillatory path. In order to give an adequate overview of the measured oscillations, three regions with a constant width in the z-direction have been defined: the mid-region (A), the outer region (B) and the overlap region (C). These regions are schematically presented in Figure 9. Based on these regions, the average dimensionless period (T^+) and the dimensionless maximum spanwise flow velocity (w_m^+) of a fluid particle can be calculated in the various domains, in analogy to the research regarding active wall oscillations. The non-dimensionalization is performed by means of the kinematic viscosity and the wall friction velocity. Various researchers have investigated active walls and have performed a parametric sweep of the two key parameters on which the drag reduction is dependent, T^+ and the dimensionless maximum wall velocity (W_m^+). The current results do not utilize a wall oscillation, therefore W_m^+ cannot be defined for the current experiments. However, by means of the laminar solution of the so called second Stokes problem (Equation 1), an equivalent maximum wall velocity can be calculated based on the measured flow characteristics. As presented in literature, the laminar solution of the second Stokes problem also shows close agreement with a Stokes layer in a turbulent boundary layer.[18,19]

$$w^+ = W_m^+ exp\left(-y^+\sqrt{\frac{\pi}{T^+}}\right) sin\left(\frac{2\pi}{T^+}t^+ - y^+\sqrt{\frac{\pi}{T^+}}\right) \tag{1}$$

In this equation, t^+ indicates dimensionless time from the start of the oscillation as scaled by the friction velocity and the kinematic viscosity. Equation 1 reduces to Equation 2 for w_m^+.

$$w_m^+ = W_m^+ exp\left(-y^+\sqrt{\frac{\pi}{T^+}}\right) \tag{2}$$

By solving Equation 2 for the dimensionless oscillation parameters and for the known dimensionless measurement plane height, the equivalent dimensionless maximum wall oscillation velocity corresponding to the current measurements can be calculated. The final surface weighted average T^+ is 135 and W_m^+ is 0.74. The current results can be compared to the numerical data on active wall oscillations. Figure 9 presents a bi-linear interpolation of the results by Quadrio as obtained from a DNS study over a channel flow.[20] As can be observed, both values of the relevant non-dimensional oscillation parameters lie in the order of magnitude of the parameters as defined in active wall oscillation research. Furthermore, interestingly, a 4% drag reduction is expected based on the current experimental oscillation parameters and an interpolation of all data by Quadrio.[20] This drag reduction is very similar to what has been measured over the current model (3.8%).[7]

It has to be noted that these results are for a channel flow with a Reynolds number based on half of the channel height and the friction velocity (Re_τ) of 200.[20] The current experimental measurements on the other hand, are performed at a flow with a Reynolds number based on δ and the friction velocity (Re_δ) of 1226. Exact quantitative comparison between the current results and the computational data therefore remains difficult. The comparison does however, give a clear indication that the order of magnitude of the oscillation parameters is similar.

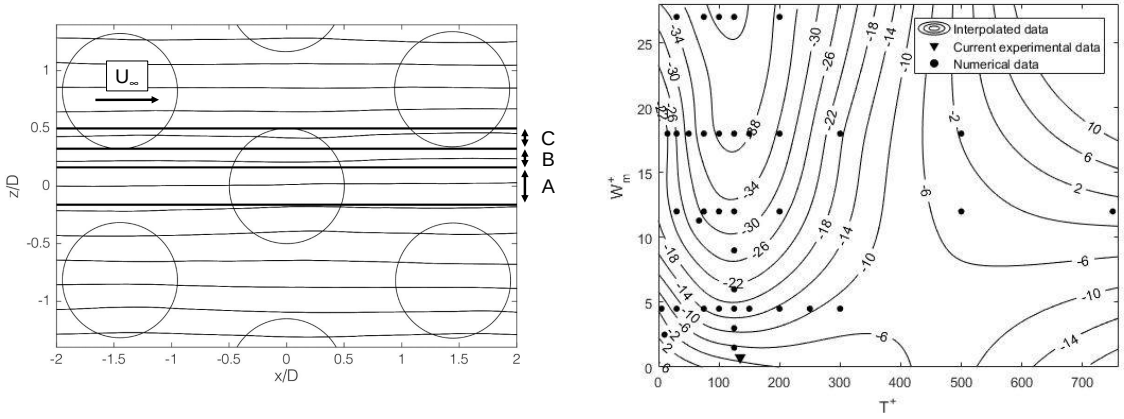

Figure 9. Streaklines of the mean velocity field over the dimpled plate (plane 1) at y/δ of approximately 0.2 (left). w-component in streaklines is amplified 5x for clarity and flat plate data subtracted. A) indicates the mid-region. B) indicates the outer region. C) indicates overlap region. The A-, B- and C-region respectively cover 39%, 39% and 22% of the local surface. Flow from the left and U_∞ = 30 m/s. Drag reduction versus T^+ and W_m^+ (right). Numerical contour value corresponds to % drag increase. Based on bi-linear interpolation of DNS data for a channel flow with Re_τ of 200.[20] Includes the weighted average based on current experimental data.

V. Conclusion

The previously measured drag reductions could not be reproduced using the same test model albeit fitted in a different way in the wind tunnel. It is reasoned that this is caused by the induced inflow FPG. In line with the "Spanwise Shear" drag reduction theory, it is concluded that a probable explanation for this difference is that the FPG from the current setup has suppressed the growth of the coherent structures in the boundary layer which has rendered the drag reducing mechanism ineffective. The dimples induce a converger-diffuser flow topology as can be observed from the surface shear streaklines. The streaklines show alternating regions were the local vector angle varies between 0 and $\pm$ 10 degrees with respect to the free stream flow direction. The converger-diffuser flow topology is measured at 0.15D above the surface. Due to the interaction of the individual dimple flow topologies, a spanwise oscillation has been observed in the flow at y/δ = 20%.

When analyzing the spanwise flow oscillations in the context of wall oscillations, for the current situation the oscillation is defined by the dimensionless variables $T^+ = 135$ and $W_m^+ = 0.74$, which are in the order of magnitude of what can be expected when considering reported numerical research on wall oscillations. The measurement of this oscillation is the first of its kind and supports the "Spanwise Shear" drag reduction theory as independently postulated by Tay and van Nesselrooij.[4,7] Lastly, it is concluded that no region of reversed shear is observed in any of the available instantaneous vector fields from the PISFV or the PIV measurements. This is in contrast to what has often been reported in literature and therefore challenges the drag reducing theories as set out by Kiknadze.[6] His hypotheses present flow reversal as a key element of the proposed drag reducing mechanism. Dimples potentially have substantial advantages over other means of passive flow control for drag reduction: they are very shallow and therefore do not require complicated cleaning or maintenance procedures, also they are not prone to wear such as riblets. Furthermore, they can easily be (retro)fitted on skin panels and do not pose substantial design restrictions, as they are very shallow. This research contributes to the understanding of the drag reducing mechanism of these dimpled surfaces. The PIV and PISFV measurements provide data that confirms a spanwise oscillation of the near-wall flow.

The fact that for the oscillation parameters in the present experiment, the previously reported drag reduction is of the same order of what can be expected when assessing numerical research regarding active wall oscillations, provides further support of this drag reducing mechanism. On the other hand, the direct force measurements have shown that the drag reduction mechanism is sensitive to flow conditions. Further research is therefore deemed necessary to understand this sensitivity and to further investigate the drag reducing mechanism.

References

[1]Abbas, A., de Vicente, J., and Valero, E., "Aerodynamic technologies to improve aircraft performance," *Aerospace Science and Technology*, Vol. 28, No. 1, 2013, pp. 100-132.

[2]Gad-el Hak, M., *Flow Control: Passive, Active, and Reactive Flow Management*, 1st ed., Cambridge University Press, New York, 2006.

[3]Spalart, P. R., and McLean, J. D., "Drag reduction: enticing turbulence, and then an industry," *Philosophical Transactions of the Royal Society of London A: Mathematical, Physical and Engineering Sciences*, Vol. 369, No. 1940, 2011, pp. 1556-1569.

[4]Tay, C. M. J., Khoo, B. C., and Chew, Y. T., "Mechanics of drag reduction by shallow dimples in channel flow," *Physics of Fluids*, Vol. 27, No. 3, 2015, 035109.

[5]Veldhuis, L. L. M., and Vervoort, E., "Drag effect of a dented surface in a turbulent flow," *Proceedings of the 27th AIAA Applied Aerodynamics Conference*, AIAA, Washington, DC, Jun. 2009, 3950.

[6]Kiknadze, G. I., Gachechiladze, I. A., Oleinikov, V. G., and Alekseev, V. V., "Mechanisms of the self-organization of tornado-like jets flowing past three-dimensional concave reliefs," *Heat Transfer Research*, Vol. 37, No. 6, 2006, pp. 467-494.

[7]van Nesselrooij, M., Veldhuis, L. L. M., van Oudheusden, B. W., and Schrijer, F. F. J., "Drag reduction by means of dimpled surfaces in turbulent boundary layers," *Experiments in Fluids*, Vol. 57, No. 9, 2016, 142.

[8]Raffel, M., Willert, C. E., Wereley, S., and Kompenhans, J., *Particle image velocimetry: a practical guide*, 1st ed., Springer-Verlag, New York, 1998.

[9]Benedict, L. H., and Gould, R. D., "Towards better uncertainty estimates for turbulence statistics," *Experiments in fluids*, Vol. 22, No. 2, 1996, pp. 129-136.

[10]Sciacchitano, A., Scarano, F., and Wieneke, B., "Multi-frame pyramid correlation for time-resolved PIV," *Experiments in fluids*, Vol. 53, No. 4, 2012, pp. 1087-1105.

[11]Mosharov, V. E., Orlov, A. A., and Radchenko, V. N., "Application of correlation analysis in surface flow visualization with oil film," *Optical Methods of Flow Investigation*, Vol. 6262, International Society for Optics and Photonics, Moscow, Jun. 2006, 62620B.

[12]Quadrio, M., and Ricco, P., "Critical assessment of turbulent drag reduction through spanwise wall oscillations," *Journal of Fluid Mechanics*, Vol. 521, Dec. 2004, pp. 251-271.

[13]Wei, L., and Pollard, A., "Direct numerical simulation of a turbulent flow with pressure gradients," *Progress in Turbulence III*, Springer-Verlag, Heidelberg, Germany, 2009, pp. 131-134.

[14]Laval, J. P., Marquillie, M., and Ehrenstein, U., "On the relation between kinetic energy production in adverse-pressure gradient wall turbulence and streak instability," *Journal of Turbulence*, Vol. 13, No. 11, 2012, pp. 1-19.

[15]Harun, Z., Monty, J. P., Mathis, R., and Marusic, I., "Pressure gradient effects on the large-scale structure of turbulent boundary layers," *Journal of Fluid Mechanics*, Vol. 715, Jan. 2013, pp. 477-498.

[16]van Campenhout, O. W. G., van Nesselrooij, M., Veldhuis, L. L. M., van Oudheusden, B. W., and Schrijer, F. F. J., "Flow visualization over drag reducing dimpled surfaces in turbulent boundary layers using particle image velocimetry," *Proceedings of the 18th international symposium on applications of laser and imaging techniques to fluid mechanics*, Springer Science & Business Media, Lisbon, Portugal, Jul. 4-7 2016, pp. 1792-1812.

[17]Tay, C. M., Chew, Y. T., Khoo, B. C., and Zhao, J. B., "Development of flow structures over dimples," *Experimental Thermal and Fluid Science*, Vol. 52, Jan. 2014, pp. 278-287.

[18]Quadrio, M., and Sibilla, S., "Numerical simulation of turbulent flow in a pipe oscillating around its axis," *Journal of Fluid Mechanics*, Vol. 424, Nov. 2000, pp. 217-241.

[19]Quadrio, M., and Ricco, P., "Initial response of a turbulent channel flow to spanwise oscillation of the walls," *Journal of Turbulence*, Vol. 4, No. 7, 2003, pp. 1-23.

[20]Quadrio, M., and Ricco, P., "Critical assessment of turbulent drag reduction through spanwise wall oscillations," *Journal of Fluid Mechanics*, Vol. 521, Jul. 2004, pp. 251-271.

This article has been cited by:

1. J. H. Ng, R. K. Jaiman, T. T. Lim, C. M. Tay, B. C. Khoo. 2020. Correction to: Geometric Effects of Shallow Dimples in Turbulent Channel Flows at $$Re_{\tau } \approx 180$$: A Vorticity Transport Perspective. *Flow, Turbulence and Combustion* **105**:1, 123-124. [Crossref]